Available online at www.sciencedirect.com
ScienceDirect
Trans. Nonferrous Met. Soc. China 32(2022) 882−894

Transactions of Nonferrous Metals Society of China
www.tnmsc.cn

Effect of hydroxyapatite:zirconia volume fraction ratio on mechanical and corrosive properties of Ti-matrix composite scaffolds

Mehmet TOPUZ[1], Burak DIKICI[2], Mehmet GAVGALI[3], Yasemin YILMAZER[4]

1. Department of Mechanical Engineering, Van Yüzüncü Yıl University, Van 65080, Turkey;
2. Department of Metallurgical and Materials Engineering, Atatürk University, Erzurum 25240, Turkey;
3. Department of Mechanical Engineering, Necmettin Erbakan University, Konya 42090, Turkey;
4. Department of Molecular Biology and Genetics, İstanbul Sabahattin Zaim University, İstanbul 34303, Turkey

Received 11 July 2021; accepted 18 November 2021

Abstract: Ti-based scaffolds reinforced with zirconia and hydroxyapatite were produced successfully by a hybrid method with an eco-friendliness and low cost to obtain low elastic modulus (*E*) with sufficient physical, electrochemical and biological properties. The effect of simultaneous modification of the volume fraction of hydroxyapatite (HA) and zirconia (ZrO_2) on scaffolds was investigated in terms of mechanical, corrosive, and antibacterial properties. Scanning electron microscopy with attached electron dispersive spectroscopy and X-ray diffraction were used for the characterization of scaffolds. Compression and electrochemical tests were performed to determine mechanical properties with detailed fracture mechanism and in-vitro corrosion susceptibility to simulated body fluid at 37 °C, respectively. Antibacterial tests were carried out by comparing the inhibition areas of *E.coli* and *S.aureus* bacteria. It was observed that the mechanical strength of the scaffolds decreased with increasing HA:ZrO_2 volume fraction ratio. The lowest *E* was achieved (6.61 GPa) in 6:4 HA:ZrO_2 composite scaffolds. Corrosion current density (J_{corr}) values were calculated to be 21, 337, and 504 $\mu A/cm^2$ for unreinforced Ti, 3:2 and 6:4 HA:ZrO_2 reinforced scaffolds, respectively. The inhibition capacity of the 6:4 reinforced composite scaffold was found to be more effective against *S.aureus* bacteria than other scaffolds.

Key words: titanium biocomposite; hydroxyapatite; zirconia; scaffold; mechanical properties; in-vitro corrosion

1 Introduction

The use of titanium (Ti) in the biomedical field has become highly popular as it provides the biomaterial requirements superior to other candidate materials (stainless steels: 316L etc., Co−Cr alloys, commercial niobium (Nb) and commercial tantalum (Ta) etc.) [1]. Briefly, these requirements are corrosion resistance, biocompatibility, bio adhesion (bone growth), elastic modulus (especially compared with other candidate materials, such as Ti: 100−120 GPa), fatigue strength and good machinability [2]. These properties especially corrosion resistance and biocompatibility make titanium the preferred candidate than others [3].

As the load on the bone decreases with the large elastic modulus (*E*) difference between the biomaterial and bone, it cannot regenerate itself due to the fact that osteoporosis occurs over time, and this phenomenon is also known as stress-shielding effect [4]. With the production of porous material, which is one of the methods used to reduce *E* value, elastic modulus of Ti (100−105 GPa) can be decreased to levels of the bone (25−35 GPa) [5,6]. Porous materials which were used as biomaterial have high absorption properties. In particular, their

---

Corresponding author: Mehmet TOPUZ, Tel: +90-432-4445065, Fax: +90-432-2251730, E-mail: mehmettopuz@yyu.edu.tr;
Burak DIKICI, Tel: +90-442-2316038, Fax: +90-442-2310000, E-mail: burakdikici@gmail.com
DOI: 10.1016/S1003-6326(22)65840-0
1003-6326/© 2021 The Nonferrous Metals Society of China. Published by Elsevier Ltd & Science Press

high absorption is important for the use of biomaterials in the body [7]. As a result, porosity not only provides a protective effect against the stress shielding problem with its ability to approach the *E* value of the bone but also increases mechanical integrity with surrounding tissues [8]. It also supports the growth of the tissues in the interior of the porosity, while helping the material to behave as a whole with the surrounding tissues [7,9,10].

High biocompatibility is important in preventing possible reactions that may occur in the first contact of a biomaterial with surrounding tissues. Undoubtedly, calcium−phosphate (Ca−P) bioceramics among the materials defined to be biocompatible are frequently used by researchers because of their similarity to bone tissue with terms of elemental and crystal structures. Hydroxyapatite (HA) is a bioceramic that constitutes almost 50% of all bone tissues and is especially important for bone tissues in terms of mechanical strength [11]. HA is frequently used in medical applications due to its major advantages such as chemical integrability with bone tissues, porous structure, high biocompatibility, and enhanced bioactivity [12,13].

When the mechanical behaviour differences between bone and HA are investigated, it is seen that HA has a limited long-term operation under continuous loads compared to bone [14]. It is stated that these differences are caused by different components such as proteins, blood vessels, red marrow, spongy bone and periosteum [7,15]. Due to the mechanical disadvantages of HA alone, the researchers concentrated their studies on HA reinforced composite structures with metallic matrix, especially Ti [16].

ERIKSSON et al [17] found that as a result of sintering at 1500 °C in bulk Ti−HA composites, the Ca in the HA transformed into $CaTiO_3$; moreover, the remaining P reacted with Ti to transform into Ti_xP_y. Similarly, POPA et al [18] revealed that the diffusion ability of Ca on Ti is more effective than P in HA-reinforced Ti−HA composites ranging from 5 to 50 wt.%. On the other hand, it has been noted that the diffusivity of P increases with increasing pressure. ZHANG et al [19] concluded that a decrease in *E* and increase in porosity in Ti−HA composite materials will increase the osteoconductivity.

As a result of the use of different phases such as zirconia (ZrO_2) with HA, its properties such as crystallization, morphology and lattice parameter could be changed. Also, this affects the physical properties of HA such as hardness, strength and wear resistance [20,21]. ZrO_2, which is mostly used in special applications such as corona applications, bridge frames and dental implant screws [22], improves the hardness, mechanical properties and abrasion resistance of HA due to its higher chemical stability and inertness [23]. ZrO_2 has a monoclinic crystal structure at room temperature and stabilizes the quadrilateral or cubic phases of other materials with heat treatments at high temperatures. Stabilized ZrO_2, also known as yttria−ZrO_2, has a wide area of use due to its high thermal, enhanced mechanical and electrical-insulation properties. For instance, yttria−ZrO_2 orthopaedic implants have the greatest value of fracture toughness. Furthermore, studies have been shown that the wear resistance of ZrO_2 is even superior to that of alumina (Al_2O_3) [24].

CHIU et al [25] emphasized that in HA−ZrO_2 composites, the ZrO_2 additive reduces the shrinkage caused by sintering, allowing the production of materials with almost the final shape. BERMÚDEZ-REYES et al [26] stated that in HA−ZrO_2 composites, sintering of the HA−Zr binary system at 1500 °C is more appropriate, but at higher sintering temperatures than 1000 °C, the HA structure decomposes and transforms into different Ca−P based bioceramics such as β-TCP. MATSUMATO et al [27] found that ZrO_2−HA composites, composed of 0 to 50 wt.% HA, have high protein absorption as well as the high affinity between composites and cells as a result of in-vivo tests.

This study was aimed on simultaneous effect of HA and ZrO_2 reinforcements ratios on Ti-based composite scaffolds. While the porosity was kept constant at nearly 40% in scaffolds, the simultaneous HA:ZrO_2 reinforcement was investigated, with terms of the characterization, mechanical properties, corrosion susceptibility and antibacterial behaviour in details.

2 Experimental

2.1 Production of scaffolds

Ti (Merck), HA (Sigma-Aldrich) and ZrO_2 irregular shaped with average sizes of 45 μm, 3−5 μm and 5−10 μm, were used as raw powders, respectively. NaCl powders with varying sizes between 150 and 550 μm were used as porogens. The total reinforcement of HA−ZrO_2 was selected as 5 and 10 vol.%, respectively, and the ZrO_2 ratio in the reinforcement was kept constant at 40 vol.%. Hereafter, the 3:2 and 6:4 (volume ratio) HA:ZrO_2 composite scaffolds were referred to as "HZ5" and "HZ10" for better clarification, respectively. In other words, it can be summarized that pure Ti, Ti/(3HA−2ZrO_2) and Ti/(6HA−4ZrO_2) were named as "T", "HZ5" and "HZ10", respectively. Ti, HA and ZrO_2 powders were mixed for 3 h with the blender (T2F, Turbula). In order to prevent possible breakings of porogens, NaCl powders were mixed with the matrix and reinforcements for a further 2 h. Cylindrical shaped hot work steel die used as a mold for *d*20 mm × 10 mm pellet (green part) production. The powder mixtures were mixed manually after feeding into the mold, to prevent agglomerations that may occur due to varied densities and sizes of the powders. Pellets were produced by hydraulic press machine under 700 MPa applied uniaxially for 5 min.

Before sintering of pellets, NaCl powders were leached in suspended and heated (70 °C) distilled water (DW) for 4 h with magnetic stirring. After leaching, porous pellets were kept at 120 °C for 8 h to evaporate residual water. Furthermore, pellets were preserved in a desiccator to prevent moisture absorption into macro/micro sized pores. Atmosphere controlled vertical tube furnace (PZF, Protherm) was used in the sintering stage. Sintering was carried out at 1000 °C for 1 h with 8 °C/min heating ramp and cooled in the furnace. Argon (Ar) gas was used continuously (1 L/min) during sintering to reduce the reaction of Ti with oxygen following DTA analysis performed in the previous study [11]. Moreover, according to the importance of Ar gas or the use of high vacuum mentioned in other studies [28], the oxygen content of 0.3 wt.% should not be exceeded. For this reason, the sintering furnace was vacuumed with 2×10^4 Pa before continuous Ar gas flow. After sintering, the samples were cut into a 5 mm × 5 mmm × 10 mm rectangular prism shape by a precision cutting machine (MICRACUT 152, Metkon). Then, samples were dried at 120 °C for 4 h in the oven (FED 115, Binder) after being cleaned with DW and ethanol for 2 and 10 min, respectively, by using an ultrasonic cleaner. Macro front and cross-section images of produced composite scaffolds are presented in Fig. 1.

2.2 Characterization

Shrinkage in the scaffolds was determined by measuring diameters and heights of scaffolds by a 1/20 mm precision calliper (MITUTOYO 530-104) before and after sintering. The experimental total porosity was calculated by using an analytical scale (PRECISA LS 220A SCS) with Archimedes' principle.

Scanning electron microscopy (SEM) was used in microstructural evaluation of scaffolds. Simultaneously, by using energy dispersive spectroscopy (EDS) attached to the SEM, scaffolds were characterized elementally. X-ray diffraction (XRD) analyses were carried out to reveal phase formation

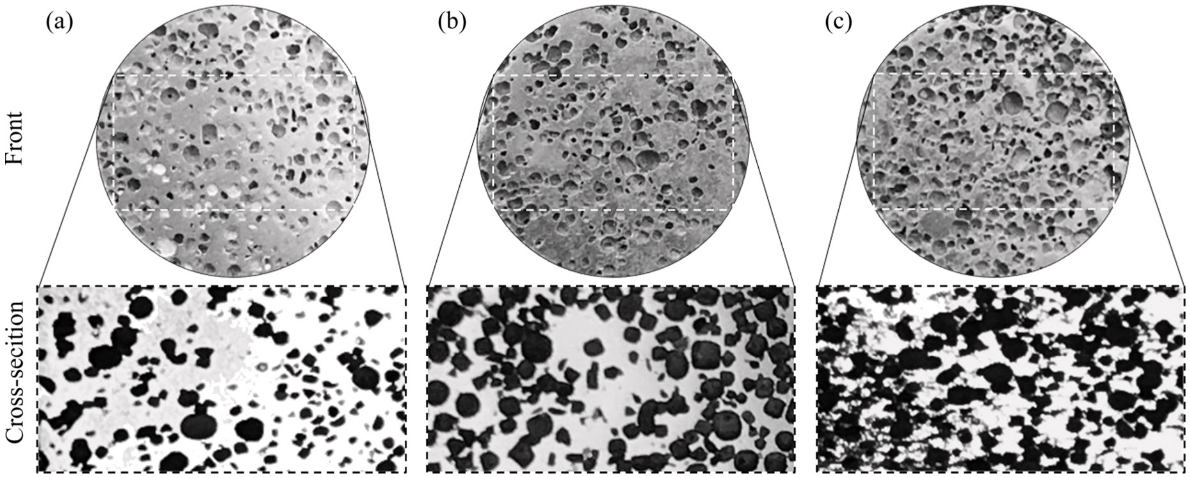

Fig. 1 Macro front and cross-section images of produced composite scaffolds: (a) T; (b) THZ5; (c) THZ10

after sintering in scaffolds. Cu K_α radiation source was used with performing at a scan speed of 0.2 (°)/s between 2θ=20° and 80°.

2.3 Compression tests

Compression tests were carried out under ISO 13314 standard by using a universal mechanical device (RAAGEN electromechanical universal testing machine) to determine the mechanical strength of the scaffolds. After tests, the mechanical properties (elastic modulus (E), plateau strength (σ_{plateau}), plateau elongation (δ_{plateau}) and yield strength (σ_{yield})) were determined from stress−strain curves. As stated in the ISO standard, E values were calculated from slope of the elastic deformation region, σ_{plateau} was obtained by calculating the average of the stresses in 20% and 40% strain, δ_{plateau} was obtained by calculating the strain difference occurring in the whole plateau region and σ_{yield} was revealed by using the 0.2% offset rule. Tests were carried out at room temperature with a compression ratio of 0.5 mm/min as specified in the ISO standard.

2.4 In-vitro corrosion tests

Corrosion tests were performed in a potentiostat/galvanostat (GAMRY PCI14/750 USA) corrosion test unit under ASTM G59 standard to reveal the corrosion behaviour of the samples. Saturated silver/silver chloride electrode (Ag/AgCl), platinum wire (Pt) and samples were used as reference electrode, counter electrode and working electrode, respectively, in the three-electrode method. The tests were carried out under in-vitro conditions (body temperature approximately 37 °C and electrolyte as simulated body fluid: SBF). The SBF electrolyte consists of NaCl, KCl, $CaCl_2$, $MgSO_4\cdot 7H_2O$, $MgCl_2\cdot 6H_2O$, $Na_2HPO_4\cdot 2H_2O$, KH_2PO_4, D-Glucose (Dextrose) and $NaHCO_3$ chemicals as specified in Hank's balanced salt solution (HBSS) [29]. The amounts of chemicals required to prepare 2000 mL of electrolyte are 16 g, 800 mg, 280 mg, 200 mg, 200 mg, 120 mg, 120 mg, 2 g and 700 mg, respectively. Open circuit potential (OCP) measurements were carried out for samples to reach equilibrium (steady state) in the electrolyte which is quite important due to the ratio, size and shape of the pores. The corrosion resistance of the scaffolds was determined by potentiodynamic polarization scanning (PDS) tests after reaching potential equilibrium. PDS was started from −1.1 V cathodic over potential by applying 1 mV/s until reaching +1.9 V anodic over potential. For in-vitro corrosion tests, the cross-sectional area of the scaffolds was kept constant at 0.42 cm^2, except for the macro and micropores on the surfaces.

2.5 Antibacterial behaviors

Firstly, scaffolds were cleaned with DW and ethanol for 3 min followed by drying in the oven at 120 °C for 30 min. Then, they were sterilized with UV light at wavelength of 254 nm for 20 min. *Escherichia coli* (*E.coli*, ATCC 25922) and *Staphylococcus aureus* (*S.aureus*, ATCC 25923) are incubated in trypticase broth at 37 °C for 2 h. After the turbidity is formed, standard turbidity is created by adjusting to McFarland 0.5 (108 micro-organisms/mL) (McFarland standards were developed to determine the number of bacteria in a liquid medium, containing degrees of turbidity equivalent to the number of bacteria cultivated). 100 μL of this suspension is taken and inoculated on the Mueller Hinton agar surface. Subsequently, scaffolds were placed on the agar surface with the help of sterile forceps. It should be paid attention to have a distance of 22 mm between the scaffolds and 14 mm from the edge of the petri dish so that the areas to be formed do not overlap. Then, the media are incubated at 37 °C for 20−24 h and the diameters of inhibition zones were measured by a digital micrometer [30].

3 Results and discussion

3.1 Microstructure

The shrinkages after the sintering of the scaffolds and the porosities as a result of the density measurements of the samples made by the Archimedes' method are presented in Fig. 2. Measurements were taken after drying at 120 °C for 8 h before sintering and after sintering at 1000 °C for 1 h.

It is seen in Fig. 2 that the shrinkages in scaffolds were decreased with the reinforcement of HA and ZrO_2 powders [18]. In other words, expansion was encountered in scaffolds together with reinforced composites and similar findings were obtained by PRANAINGRUM et al [31]. It is thought that this expansion prevents the shrinkage of Ti as a result of HA and ZrO_2 reinforcements,

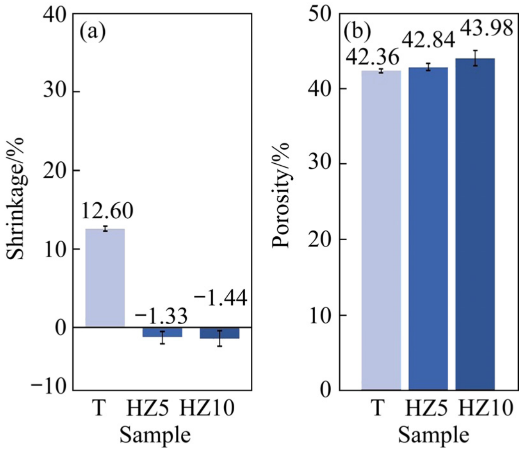

Fig. 2 Shrinkages (a) and experimental porosities (b) after production of scaffolds

since the reinforcements agglomerating around the matrix powders will prevent the sintering of the metal Ti powders. On the other hand, reduced shrinkage with HA−ZrO_2 reinforcements may be a result of *t*-ZrO_2 and *m*-ZrO_2 transformations stated by AYOUB et al [32]. When the porosities are considered, it is thought that despite 40 vol.% theoretical porosity, excessive porosity up to 3.98 vol.% is encountered in scaffolds that may have occurred from the micropores formation. Higher porosity may have encountered due to undissolved NaCl in scaffolds. On the other hand, other formation mechanism of micropores is that the necks among the powders are not completely closed as a result of insufficient pressing and/or insufficient sintering, which is the nature of the powder metallurgy [33]. With the higher content of ZrO_2 reinforcement, the total porosity in scaffolds has slightly increased due to the insufficient neck growth as a result of high stability of Ti−ZrO_2 during sintering [34]. If both shrinkages and porosity are considered together, it is thought that the increased porosity may have occurred as a result of the decreased shrinkages as well as the low sinterability, especially with HA−ZrO_2 composite scaffolds.

SEM surface morphologies of scaffolds and EDX analysis results showing their elemental distribution are presented in Fig. 3.

From the SEM images, no irregularities were found on porous surfaces, especially around or inner surface of the pore in Ti scaffolds. On the other hand, composite scaffolds have micropores that spread around and inner-walls of macropores. Moreover, as stated by ANAWATI et al [35], it is predicted that the pores on the surface may break off from the surface during the surface preparation process of HA reinforced Ti/HA composites. Another thought is that the micropores that increase with the increased reinforcement content may result from the low sinterability. It is known that ceramic particles have higher sintering temperatures compared to metallic particles, and act as sintering inhibitor. On the other hand, it was stated by MONDAL et al [36] that these micropores can support bone tissue growth. EDX results are taken from areas representing Ti, HZ5 and HZ10, respectively, and reveal the elemental distributions on scaffolds. Only Ti element was encountered in the Ti scaffold, while in HZ5 and HZ10 scaffolds, elements such as Ca, P and Zr representing the reinforcements, Na and Cl due to NaCl used as a space holder and Si element originated from the colloidal silica treatment during polishing were found. The low peak intensity of Ca, P and Zr elements in EDX analysis is attributed to the low sintering capability of reinforcements (HA−ZrO_2) and Ti [11], and these elements can also easily be removed from the surface during surface preparation.

Figure 4 shows the XRD results of the T, HZ5 and HZ10 scaffolds.

From the XRD analyses, after sintering, the α-Ti phase, which forms the matrix of 90 and 95 vol.% of scaffolds, was observed to be dominant. HA, NaCl and Ti_5P_3 peaks were observed in scaffolds. It is thought that the NaCl peak may be caused by the trace amount of NaCl remaining undissolved in the macroporous [6], as well as during the washing of the samples with deionized water. The reason for the absence of the ZrO_2 phase is thought to be due to the low fractions of ZrO_2. Moreover, the fact that the powders are not filled homogeneously into the mold before pressing can also have such consequences. The Ti_5P_3 peak indicates that P in HA reacts with Ti with a diffusion mechanism which starts with the loss of the hydroxyl chain of HA during sintering and results in Ti_xP_y as a result of a series of reactions defined by ARIFIN et al [37].

3.2 Compression properties

Compression test results of scaffolds are given in Fig. 5.

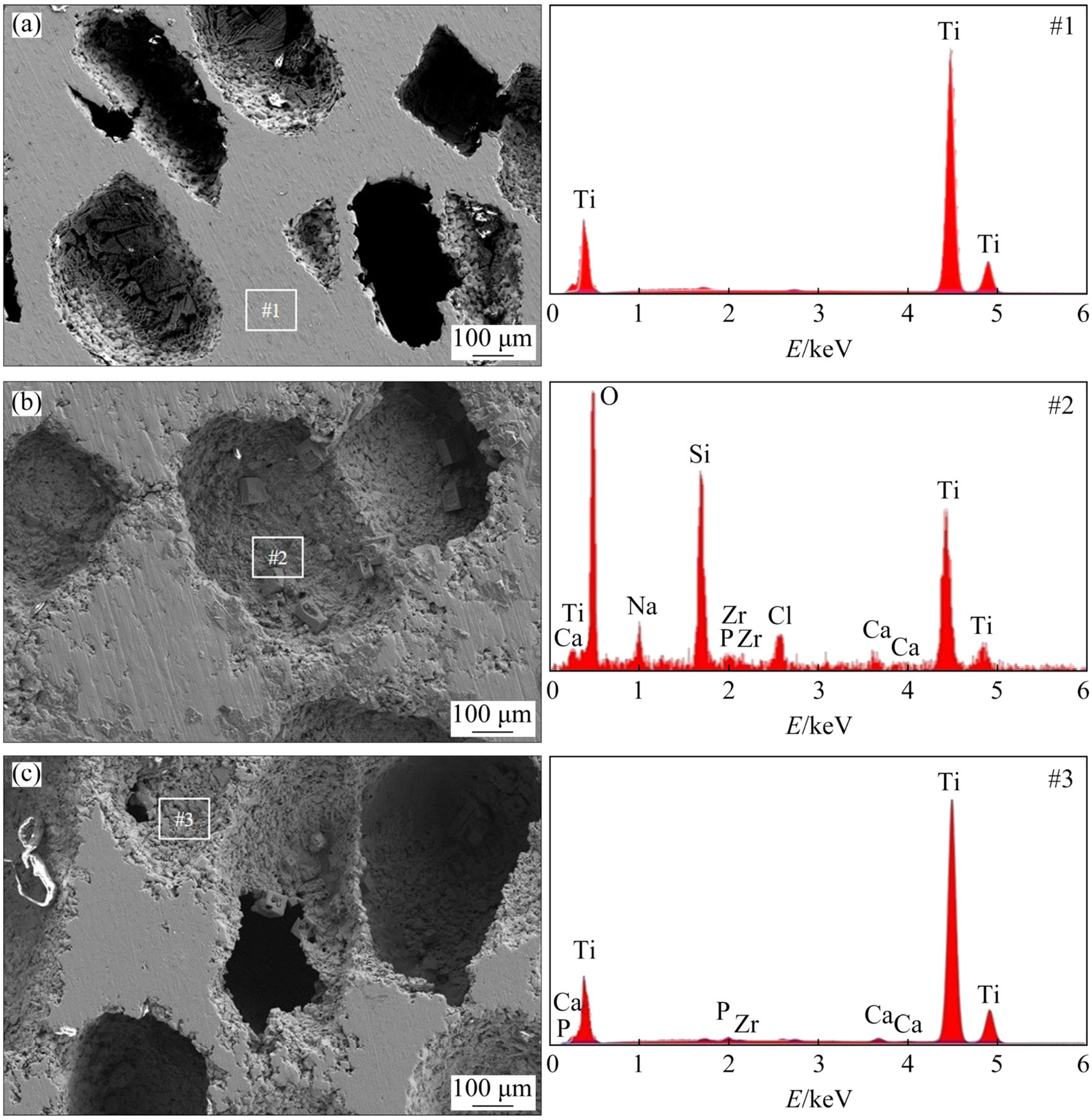

Fig. 3 SEM surface morphologies with detailed macro porosities and EDX elemental distributions along surface and porosities of T (a), HZ5 (b) and HZ10 (c)

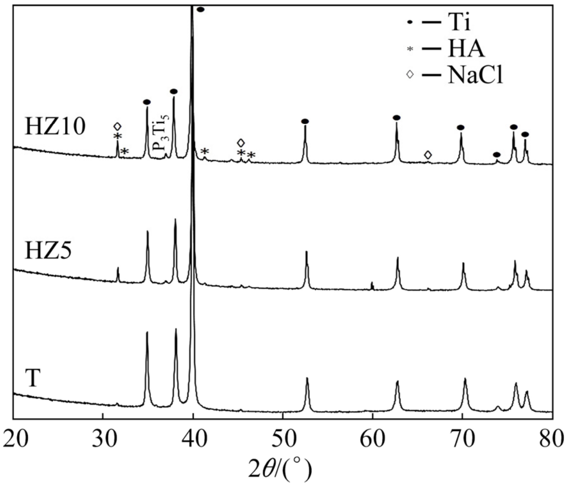

Fig. 4 XRD patterns of 40 vol.% porous scaffolds after sintering

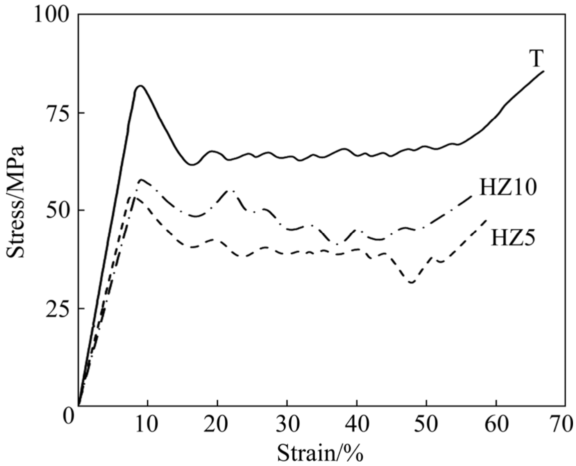

Fig. 5 Compression results of 40% porous scaffolds, 1:2 ratio rectangular samples (width: 5 mm and height: 10 mm) according to ISO 13314 standard

While *E* values tended to decrease with increased content of reinforcement in scaffolds, σ_{yield} value increased in HZ10 scaffolds. *E* values for T, HZ5 and HZ10 were measured to be 9.94, 7.32 and 6.61 GPa, respectively. Such low *E* values will make a great contribution to prevent the stress shielding effect [38]. On the other hand, it is important to provide sufficient mechanical rigidity. The σ_{yield} values were calculated to be 81.23, 53.13 and 57.34 MPa for T, HZ5 and HZ10, respectively. By the way, it has been stated by many researchers that the contribution of ZrO_2 reinforcement leading to dispersion hardening in the Ti matrix increased the σ_{yield} value [23,39]. A stress−strain curve has been obtained, which is unique to porous materials that deform the macropores and then progresses in the form of load transfer to other macropores through micropores [40]. While σ_{plateau} also had a trend similar with the σ_{yield} of scaffolds (63.86, 39.37 and 47.58 MPa for T, HZ5 and HZ10, respectively), δ_{plateau} decreased with HZ5 and HZ10 like *E* of scaffolds (39.14, 35.74 and 33.17% for T, HZ5 and HZ10, respectively). As a result of the HZ10 scaffold having higher toughness than HZ5, it has been revealed that the plastic deformability is increased with ZrO_2 reinforcement [41].

In Figs. 6(a, b, c), SEM morphologies of fracture surfaces after compression tests for T, HZ5 and HZ10, respectively, are presented.

Cleavage patterns specific to shear stress can be seen in Fig. 6(a). These patterns encountered in all scaffolds indicate that the fracture mechanism progresses transgranular with limited trans-intergranular [11]. Figure 6(b) shows a decrease in the neck cross-sectional area of the HZ5 scaffold compared to the T scaffold. In the fracture morphology of the HZ10 scaffold, neck points were considerably reduced and more intergranular breaks were observed (Fig. 6(c)). The area reduction in transgranular fracture surfaces is the evidence of the σ_{plateau} values of composite scaffolds in Fig. 5. Intergranular fracture surface can be caused by decreasing sintering capability with increasing reinforcement content. Another important finding is that NaCl hollow pores are found, confirmed with EDX analyses in macropores on fracture surfaces (Figs. 6(a, b)). KUMAR et al [42] predicted that these hollow fractured particles will increase fracture toughness as a result of the increase in the fracture path length. On the other hand, a fracture mechanism was observed similar to the research by MATSUMOTO et al [27]. Briefly, as the amount of porosity increases, a fracture mechanism that continues through windows (connection among macropores) and loses scaffold's integrity has dominant fracture mechanism [11,43].

3.3 In-vitro corrosion properties

In Fig. 7, PDS results of scaffolds with 40% porosity are presented with OCP.

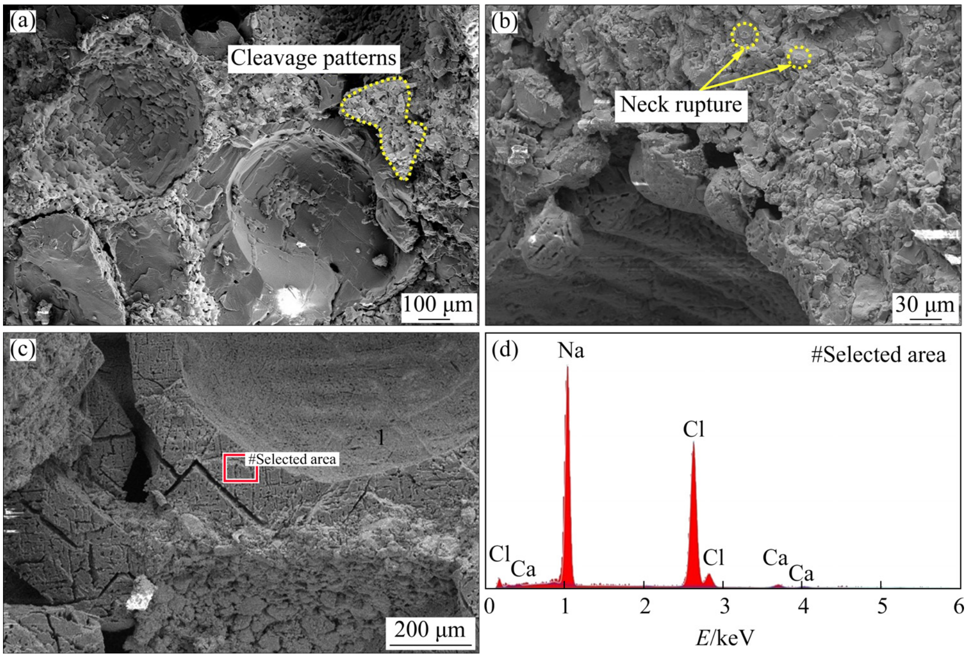

Fig. 6 SEM morphologies of fractured surfaces of scaffolds after compression tests: (a) T; (b) HZ5; (c) HZ10; (d) EDX result of selected area in (c)

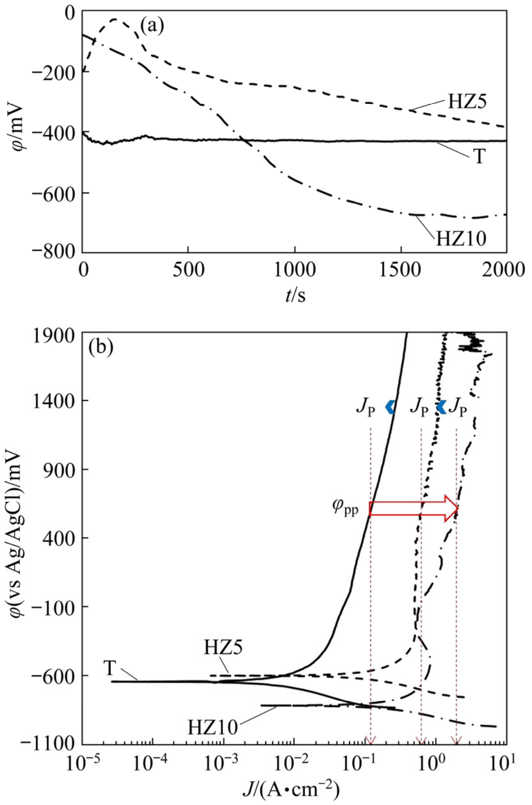

Fig. 7 In-vitro corrosion test results with scaffolds immersed in SBF electrolyte: (a) OCP curve; (b) PDS curve

As can be understood from the results of OCP, while the static equilibrium state was reached in a short time (2000 s) with increasing time in T scaffolds, a noisy potential change was observed in the HZ5 and HZ10 scaffolds. The reason for this is thought to consist of different factors such as powder metallurgy and micropores resulting from insufficient sintering and reinforcement content. It was foreseen from PDS curves that the corrosion potential ($\varphi_{\rm corr}$) values of the T samples visibly decrease, unlike the composite scaffolds. This can be interpreted by ANAWATI et al [35] that the corrosion resistance decreases with the reinforcement type and ratio similarly. Increased potential resulted in passivation in the anodic branch on all samples [44]. This phenomenon is frequently observed in Ti and Ti-based composite materials [45]. It is thought that these fluctuations in anodic branches may have occurred as a result of the formation and break of the oxide film formed on the surfaces [46]. On the other hand, it is seen that within the same passivation potential ($\varphi_{\rm pp}$, red arrow in Fig. 7), Ti has lower passive current density ($J_{\rm p}$) values (dashed lines in Fig. 7) than composite scaffolds. This can be interpreted that passivation as seen in anodic branch, is less stable in composite scaffolds due to different corrosion kinetics of reinforcements during tests. Another suggested mechanism was that increased microporosity led to increased electrolyte contacts, resulting in the formation of microdischarges and discontinuity of oxide film in SBF electrolyte [47].

For more detailed corrosion investigations, some important corrosion parameters were obtained from the PDS curves in line with the ASTM G59−97 Standard and are presented in Table 1. Polarization resistances ($R_{\rm p}$) were calculated using the Stern-Geary coefficient (B), related to the anodic ($\beta_{\rm a}$) and cathodic ($\beta_{\rm c}$) by Tafel slopes.

In Table 1, $\varphi_{\rm corr}$ values reveal the potential behaviour of the samples in the electrolyte, while $J_{\rm corr}$ values reveal the corrosion resistance of the samples in Hank's electrolyte, in other words, their sensitivity. The $J_{\rm corr}$ values of T, HZ5 and HZ10 were 21, 337 and 504 μA/cm^2, respectively. When $J_{\rm corr}$ values are compared, it has been confirmed that T has higher corrosion resistance in all scaffolds. Polarization resistance ($R_{\rm p}$) values also showed similar results which were inversely proportional to $J_{\rm corr}$ and corrosion. rates. In other words, higher $R_{\rm p}$ means lower $J_{\rm corr}$ and corrosion rates (5496.43, 264.36 and 135.26 Ω/cm^2 for T, HZ5 and HZ10, respectively). It is thought that the electrolyte creates a stable region, especially in micropores, and aggressive ions such as Cl$^-$ reduce the corrosion resistance of composite scaffolds [48]. On the other hand, as a result of the decreased sinterability, the aggressiveness of Cl$^-$ ions increases [49]. As can be seen from the corrosion

Table 1 Some important corrosion parameters calculated from PDS curves in accordance with ASTM G59—97 standard

Sample	$\varphi_{\rm corr}$/mV	$J_{\rm corr}$/(μA·cm^{-2})	Corrosion rate/mpy	$\beta_{\rm a}$/(V·decade^{-1})	$\beta_{\rm c}$/(V·decade^{-1})	$R_{\rm p}$/(Ω·cm^{-2})
T	−642.00	21	7.83	1.45	0.32	5496.43
HZ5	−599.00	337	110.20	1.17	0.25	264.36
HZ10	−817.00	504	207.10	1.05	0.18	135.26

data in Table 1, it has been revealed that the scaffolds exhibit different electrochemical behaviours with both different compositions and porosities. These differences are predicted to be due to the following parameters: (1) pressing pressure, (2) sintering temperature and time, (3) compositions, (4) macropores/micropores content, (5) electrolyte content, and (6) homogeneity of the reinforcement, etc.

SEM surface morphologies performed to reveal the destruction of scaffolds after in-vitro corrosion tests are presented in Fig. 8.

Localized and less corroded areas on the surface were observed in the T scaffolds (Fig. 8(a)). Corroded areas occurring from the surface may result from the powder metallurgy or from the edge of the randomly distributed macropore that may locate under the corroded area. On the other hand, around the macropores on the HZ5 composite scaffold, corrosion products formed as a result of many different ions in Hank's electrolyte were found brightly (Fig. 8(b)). Surprisingly, in the HZ10 composite scaffold, the corrosion mechanism was encountered as extending through the macropores (Fig. 8(c)). In this state, the corrosion morphology of the HZ10 can be interpreted as over-polarization of the HZ5. But increased corrosion rate with HZ10 may be a result of the insufficient neck growth and sintering capability, as seen in Figs. 3 and 6. Moreover, increased galvanic irregularity with increased reinforcement content may have led to an increase of J_{corr} in HZ10 composite scaffold. The edges of the macropores in the HZ5 scaffold may have served as the initiation of corrosion. Briefly, with increasing the reinforcement content (HZ10), macropore edges may act as anode with the potential increase as a result of the agglomeration of HA and ZrO_2. Another phenomenon is that this post corrosion morphology seen in HZ10 may be selective corrosion zones due to phases with different thermal expansion coefficient such as Ti_5P_3 [37].

3.4 Antibacterial properties

In Fig. 9, antibacterial behaviors of scaffolds against gram-positive and gram-negative bacterial

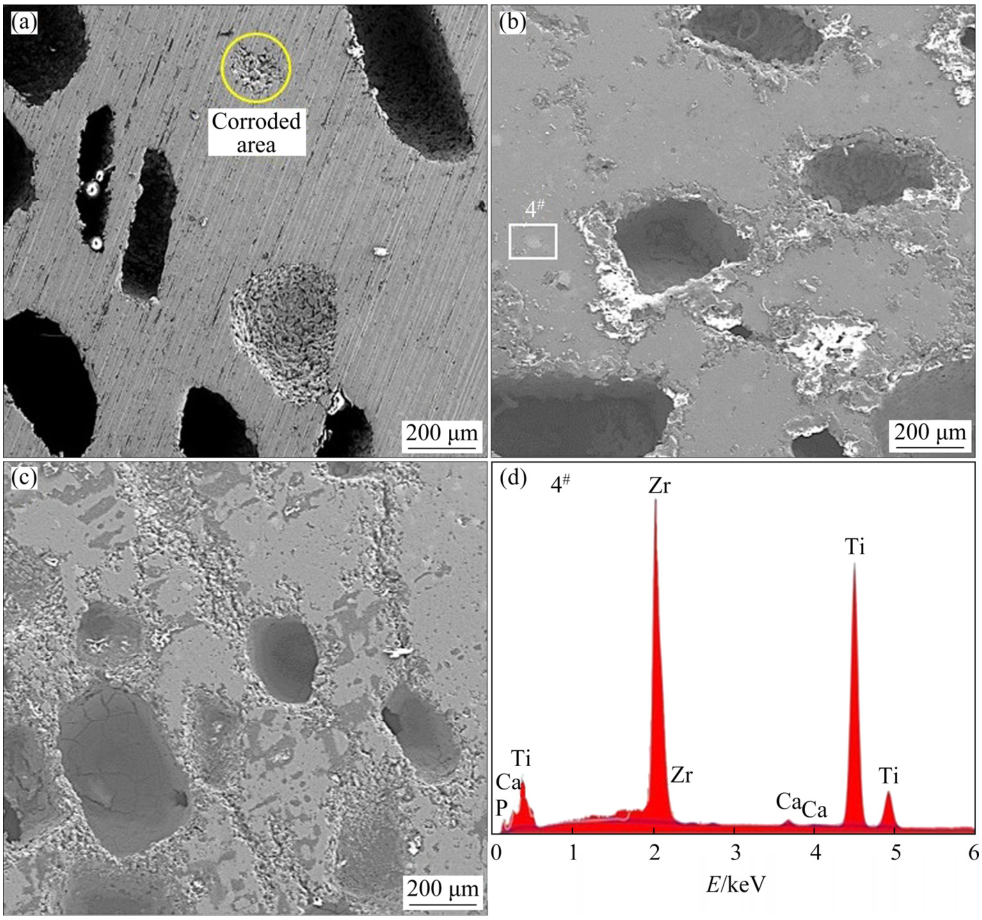

Fig. 8 Post surface examination of corroded scaffolds after in-vitro corrosion tests: (a) T; (b) HZ5; (c) HZ10; (d) EDX result of Area 4# in (b)

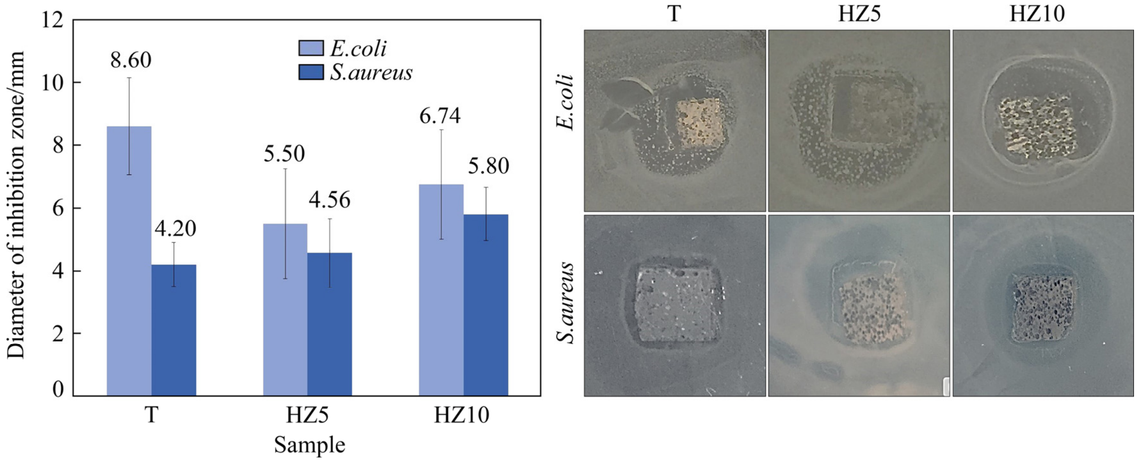

Fig. 9 Bacterial inhibition of scaffolds against both *E.coli* and *S.aureus*

species are demonstrated. After the tests, the behaviors of scaffolds against *E.coli* and *S.aureus* bacteria in the inhibition zone areas are presented visually.

All of the scaffolds appear to have an inhibition, that is an antibacterial effect, against both *E.coli* and *S.aureus* bacteria. As well known, pure titantium has a natural passive titanium dioxide (TiO_2) layer on the surface. It is reported that TiO_2 has antibacterial properties because of photocatalytic activity [50−53]. TiO_2 generates reactive oxygen species (ROS) on its surface during the process of photocatalysis when it is exposed to light at an appropriate wavelength. Bacteria wall and membranes can be deadly affected by ROS. Photocatalytic TiO_2 displayed cell inactivation at regulatory network and signaling levels, an important decrease in the activity of respiratory chain, and inhibition in the assimilation and transportation iron and phosphorous [54,55]. However, it has been observed that it has a more inhibitory effect against *E.coli* bacteria. It was observed that the HZ reinforcement increased the inhibition area against both *E.coli* and *S.aureus* bacteria, and in other words, the antibacterial behaviours were enhanced. This phenomenon may arise due to HA damage to the bacterial cytoplasmic membrane, protein denaturation, and damage to the bacteria DNA. ZrO_2 inhibits bacterial colonisation. ZrO_2 binds to the bacterial cell wall and cell membrane and inhibits the respiration process [56]. Areas of inhibition against *E.coli* (gram-negative) increased with increased reinforcements against T, HZ5 and HZ10 scaffolds, 8.60, 5.50 and 6.74 mm, respectively. For *S.aureus* (gram-positive) bacteria T, HZ5 and HZ10 were determined to be 4.20, 4.56, and 5.80 mm for scaffolds, respectively. As can be seen from the macro photos in Fig. 9, there are zones where the bacteria in the petri dish containing scaffolds cannot multiply and lose their vitality around the sample. It can be said that all of the scaffolds have an antibacterial effect since all the results have the behavior of inhibiting bacterial viability. HZ10 composite scaffold appears to have a more effective inhibition ability for *S.aureus* bacteria, which is found in one out of three people and has high antibiotic resistance [57].

4 Conclusions

(1) While the shrinkage decreased with the composite structure, it decreased even more with the increasing reinforcement content. Experimental porosity increased with increasing reinforcement content in composite scaffolds. The presence of micropores was revealed by SEM micrographs with increased reinforcement content. Energy scattering of matrix and reinforcements where Ti, Ca, P and Zr dispersed on the surface, was proven with EDX analyses. As a result of the XRD analysis, Ti, HA, NaCl, and Ti_5P_3 phases were found in XRD analysis after sintering of scaffolds.

(2) It has been determined that while both σ_{yield} and σ_{plateau} decrease with the composite scaffolds (HZ5, 53.13 and 39.37 MPa) compared to Ti scaffolds (8.23 and 63.86 MPa), the mechanical properties increase with the increased reinforcement (HZ10, 57.34 and 47.58 MPa). Fracture surfaces revealed that both transgranular and intergranular fractures were observed together in Ti/HA−ZrO_2

composite scaffolds while transgranular fracture was encountered in Ti scaffolds.

(3) PDS results showed that with HA−ZrO_2 reinforcement, J_{corr} values increased (337.0 and 504.0 μA/cm^2), and in other words, composite scaffolds have higher corrosion susceptibilities than Ti scaffold (20.9 μA/cm^2).

(4) It was revealed with antibacterial test results that all scaffolds inhibit both *E.coli* and *S.aureus* bacteria, especially HZ10 composite scaffold for *S.aureus*.

Acknowledgments

The authors are grateful for the financial supports from the Research Fund of Atatürk University, Turkey (No. FDK-2019-7281).

References

[1] OLDANI C, DOMINGUEZ A. Titanium as a biomaterial for implants [M]. London: IntechOpen, 2012.

[2] RALPH B. Titanium alloys: An atlas of structures and fracture features [M]. Boca Raton: CRC Press, 2008.

[3] LÜTJERING G, WILLIAMS J C. Special properties and applications of titanium [M]. 2nd ed. Berlin: Springer-Verlag, 2007.

[4] OTSUKI B, TAKEMOTO M, FUJIBAYASHI S, NEO M, KOKUBO T, NAKAMURA T. Pore throat size and connectivity determine bone and tissue ingrowth into porous implants: Three-dimensional micro-CT based structural analyses of porous bioactive titanium implants [J]. Biomaterials, 2006, 27: 5892−5900.

[5] NIINOMI M. Recent research and development in titanium alloys for biomedical applications and healthcare goods [J]. Science and Technology of Advanced Materials, 2003, 4: 445−454.

[6] TORRES Y, TRUEBA P, PAVÓN J J, CHICARDI E, KAMM P, GARCÍA-MORENO F, RODRIGUEZ-ORTIZ J A. Design, processing and characterization of titanium with radial graded porosity for bone implants [J]. Materials and Design, 2016, 110: 179−187.

[7] MOUR M, DAS D, WINKLER T, HOENIG E, MIELKE G, MORLOCK M M, SCHILLING A F. Advances in porous biomaterials for dental and orthopaedic applications [J]. Materials (Basel), 2010, 3: 2947−2974.

[8] DUNAND D C. Processing of titanium foams [J]. Advanced Engineering Materials, 2004, 6: 369−376.

[9] ZHENG J P, CHEN L J, CHEN D Y, SHAO C S, YI M F, ZHANG B. Effects of pore size and porosity of surface-modified porous titanium implants on bone tissue ingrowth [J]. Transactions of Nonferrous Metals Society of China, 2019, 29: 2534−2545.

[10] WANG G H, FU H, ZHAO Y Z, ZHOU K C, ZHU S H. Bone integration properties of antibacterial biomimetic porous titanium implants [J]. Transactions of Nonferrous Metals Society of China, 2017, 27: 2007−2014.

[11] TOPUZ M, DIKICI B, GAVGALI M. Titanium-based composite scaffolds reinforced with hydroxyapatite−zirconia: Production, mechanical and in-vitro characterization [J]. Journal of the Mechanical Behavior of Biomedical Materials, 2021, 118: 104480.

[12] BEST S M, PORTER A E, THIAN E S, HUANG J. Bioceramics: Past, present and for the future [J]. Journal of the European Ceramic Society, 2008, 28: 1319−1327.

[13] CASTKOVA K, HADRABA H, MATOUSEK A, ROUPCOVA P, CHLUP Z, NOVOTNA L, CIHLAR J. Synthesis of Ca,Y−zirconia/hydroxyapatite nanoparticles and composites [J]. Journal of the European Ceramic Society, 2016, 36: 2903−2912.

[14] YILMAZ E, KABATAŞ F, GÖKÇE A, FINDIK F. Production and characterization of a bone-like porous Ti/Ti−hydroxyapatite functionally graded material [J]. Journal of Materials Engineering and Performance, 2020, 29: 6455−6467.

[15] de VASCONCELLOS L M R, OLIVEIRA F N, de OLIVEIRA LEITE D, de VASCONCELLOS L G O, do PRADO R F, RAMOS C J, de ALENCASTRO GRAÇA M L, CAIRO C A A, CARVALHO Y R. Novel production method of porous surface Ti samples for biomedical application [J]. Journal of Materials Science: Materials in Medicine, 2012, 23: 357−364.

[16] HUAN Z, CHANG J. Novel bioactive composite bone cements based on the β-tricalcium phosphate−monocalcium phosphate monohydrate composite cement system [J]. Acta Biomaterialia, 2009, 5: 1253−1264.

[17] ERIKSSON M, ANDERSSON M, ADOLFSSON E, CARLSTRÖM E. Titanium–hydroxyapatite composite biomaterial for dental implants [J]. Powder Metallurgy, 2006, 49: 70−77.

[18] POPA C, SIMON V, VIDA-SIMITI I, BATIN G, CANDEA V, SIMON S. Titanium−hydroxyapatite porous structures for endosseous applications [J]. Journal of Materials Science: Materials in Medicine, 2005, 16: 1165−1171.

[19] ZHANG L, HE Z Y, ZHANG Y Q, JIANG Y H, ZHOU R. Rapidly sintering of interconnected porous Ti−HA biocomposite with high strength and enhanced bioactivity [J]. Materials Science and Engineering C, 2016, 67: 104−114.

[20] AN S H, MATSUMOTO T, MIYAJIMA H, NAKAHIRA A, KIM K H, IMAZATO S. Porous zirconia/hydroxyapatite scaffolds for bone reconstruction [J]. Dental Materials, 2012, 28: 1221−1231.

[21] TOPUZ M, DIKICI B, GÜNGÖR KOÇ S, YILMAZER H, NIINOMI M, NAKAI M. Corrosion susceptibilities of hydroxyapatite (HA) based zirconia reinforced bioactive hybrid coatings [J]. E-Journal of New World Sciences Academy, 2017, 12: 66−77.

[22] ZHANG J, IWASA M, KOTOBUKI N, TANAKA T, HIROSE M, OHGUSHI H, JIANG D. Fabrication of hydroxyapatite−zirconia composites for orthopedic applications [J]. Journal of the American Ceramic Society, 2006, 89: 3348−3355.

[23] GAIN A K, ZHANG L, LIU W. Microstructure and material properties of porous hydroxyapatite−zirconia nanocomposites using polymethyl methacrylate powders [J]. Materials and

Design, 2015, 67: 136−144.

[24] MASONIS J L, BOURNE R B, RIES M D, MCCALDEN R W, SALEHI A, KELMAN D C. Zirconia femoral head fractures: A clinical and retrieval analysis [J]. Journal of Arthroplasty, 2004, 19: 898−905.

[25] CHIU C Y, HSU H C, TUAN W H. Effect of zirconia addition on the microstructural evolution of porous hydroxyapatite [J]. Ceramics International, 2007, 33: 715−718.

[26] BERMÚDEZ-REYES B, del REFUGIO LARA-BANDA M, REYES-ZARATE E, ROJAS-MARTÍNEZ A, CAMACHO A, MONCADA-SAUCEDO N, PEREZ-SILOS V, GARCIA-RUIZ A, GUZMAN-LOPEZ A, PENA-MARTINEZ V, LARA-ARIAS J, TORRES-MENDEZ S, FUENTES-MERA L. Effect on growth and osteoblast mineralization of hydroxyapatite−zirconia (HA−ZrO_2) obtained by a new low temperature system [J]. Biomedical Materials, 2018, 13: 035001.

[27] MATSUMATO T J, AN S H, ISHIMOTO T, NAKANO T, MATSUMOTO T, IMAZATO S. Zirconia−hydroxyapatite composite material with micro porous structure [J]. Dental Materials, 2011, 27: e205−212.

[28] LAPTEV A, BRAM M, BUCHKREMER H P, STÖVER D. Study of production route for titanium parts combining very high porosity and complex shape [J]. Powder Metallalurgy, 2004, 47: 85−92.

[29] HBSS (Hank's Balanced Salt Solution) Preparation and Recipe [S]. Sunnyvale, California, AAT Bioquest, 2021.

[30] BALOUIRI M, SADIKI M, IBNSOUDA S K. Methods for in vitro evaluating antimicrobial activity: A review [J]. Journal of Pharmaceutical Analysis, 2016, 6: 71−79.

[31] PRANANINGRUM W, TOMOTAKE Y, NAITO Y, BAE J, SEKINE K, HAMADA K, ICHIKAWA T. Application of porous titanium in prosthesis production using a moldless process: Evaluation of physical and mechanical properties with various particle sizes, shapes, and mixing ratios [J]. Journal of the Mechanical Behavior of Biomedical Materials, 2016, 61: 581−589.

[32] AYOUB G, VELJOVIC D, ZEBIC M L, MILETIC V, PALCEVSKIS E, PETROVIC R, JANACKOVIC D. Composite nanostructured hydroxyapatite/yttrium stabilized zirconia dental inserts—The processing and application as dentin substitutes [J]. Ceramics Internattional, 2018, 44: 18200−18208.

[33] ESEN Z, BOR Ş. Characterization of Ti−6Al−4V alloy foams synthesized by space holder technique [J]. Materials Science and Engineering A, 2011, 528: 3200−3209.

[34] TSENG W J, HSU K T. Macroporous ZrO_2/Ti composite foams by aqueous gelcasting of particle-stabilized emulsions [J]. Advanced Powder Technology, 2016, 27: 839−844.

[35] ANAWATI, TANIGAWA H, ASOH H, OHNO T, KUBOTA M, ONO S. Electrochemical corrosion and bioactivity of titanium−hydroxyapatite composites prepared by spark plasma sintering [J]. Corrosion Science, 2013, 70: 212−220.

[36] MONDAL D P, PATEL M, JAIN H, JHA A K, DAS S, DASGUPTA R. The effect of the particle shape and strain rate on microstructure and compressive deformation response of pure Ti-foam made using acrowax as space holder [J]. Materials Science and Engineering A, 2015, 625: 331−342.

[37] ARIFIN A, SULONG A B, MUHAMAD N, SYARIF J, RAMLI M I. Material processing of hydroxyapatite and titanium alloy (HA/Ti) composite as implant materials using powder metallurgy: A review [J]. Materials and Desing, 2014, 55: 165−175.

[38] YE B, DUNAND D C. Titanium foams produced by solid-state replication of NaCl powders [J]. Materials Science and Engineering A, 2010, 528: 691−697.

[39] HAN C, LI Y C, LIANG X G, CHEN L P, ZHAO N, ZHU X K. Effect of composition and sintering temperature on mechanical properties of ZrO_2 particulate-reinforced titanium-matrix composite [J]. Transactions of Nonferrous Metals Society of China, 2012, 22: 1855−1859.

[40] ISO 13314. Mechanical testing of metals, ductility testing, compression test for porous and cellular metals [S]. 2011.

[41] ABD-ELWAHED M S, IBRAHIM A F, REDA M M. Effects of ZrO_2 nanoparticle content on microstructure and wear behavior of titanium matrix composite [J]. Journal of Materials Research and Technology, 2020, 9: 8528−8534.

[42] KUMAR R, PRAKASH K H, CHEANG P, KHOR K A. Microstructure and mechanical properties of spark plasma sintered zirconia−hydroxyapatite nano-composite powders [J]. Acta Materialia, 2005, 53: 2327−2335.

[43] TOPUZ M, DIKICI B, GAVGALI M, KASEEM M. Processing of Ti/(HA+ZrO_2) biocomposite and 50% porous hybrid scaffolds with low Young's modulus by powder metallurgy: Comparing of structural, mechanical, and corrosion properties [J]. Materials Today Communications, 2021, 29: 102813.

[44] ESEN Z, DIKICI B, DUYGULU O, DERICIOGLU A F. Titanium–magnesium based composites: Mechanical properties and in-vitro corrosion response in Ringer's solution [J]. Materials Science and Engineering A, 2013, 573: 119−126.

[45] DIKICI B, NIINOMI M, TOPUZ M, KOC S G, NAKAI M. Synthesis of biphasic calcium phosphate (BCP) coatings on β-type titanium alloys reinforced with rutile-TiO_2 compounds: Adhesion resistance and in-vitro corrosion [J]. Journal of Sol−gel Science and Technology, 2018, 87: 713−724.

[46] SCHULTZE J W, LOHRENGEL M M. Stability, reactivity and breakdown of passive films: Problems of recent and future research [J]. Electrochimica Acta, 2000, 45: 2499−2513.

[47] LEE K M, JUNG B K, KO Y G, SHIN D H. Electrochemical response of ZrO_2 incorporated titanium oxide film [J]. Materials Research Innovations, 2014, 18: S2-407−S2-410.

[48] SAY Y, AKSAKAL B, DIKICI B. Effect of hydroxyapatite/SiO_2 hybride coatings on surface morphology and corrosion resistance of REX-734 alloy [J]. Ceramics International, 2016, 42: 10151−10158.

[49] DIKICI B, NIINOMI M, TOPUZ M, SAY Y, AKSAKAL B, YILMAZER H, NAKAI M. Synthesis and characterization of hydroxyapatite/TiO_2 coatings on the β-type titanium alloys with different sintering parameters using sol−gel method [J]. Protection of Metals and Physical Chemistry of Surfaces, 2018, 54: 457−462.

[50] CHUNG I M, PARK I, SEUNG-HYUN K, THIRUVENGADAM M, RAJAKUMAR G. Plant-mediated

synthesis of silver nanoparticles: Their characteristic properties and therapeutic applications [J]. Nanoscale Research Letters, 2016, 11: 1−14.

[51] BUI A K T, BACIC A, PETTOLINO F. Polysaccharide composition of the fruit juice of Morinda citrifolia (noni) [J]. Phytochemistry, 2006, 67: 1271−1275.

[52] RAVIKUMAR P, KUMAR S S. Antifungal activity of extracellularly synthesized silver nanoparticles from Morinda citrifolia L [J]. International Journal of Technical Research and Applications, 2014, 2: 108−111.

[53] INBATHAMIZH L, PONNU T M, MARY E J. In vitro evaluation of antioxidant and anticancer potential of Morinda pubescens synthesized silver nanoparticles [J]. Journal of Pharmacy Research, 2013, 6: 32−38.

[54] ZHANG Q H, YAN X, SHAO R, DAI H L, LI S P. Preparation of nano-TiO_2 by liquid hydrolysis and characterization of its antibacterial activity [J]. Journal of Wuhan University of Technology (Materials Science Edition), 2014, 29: 407−409.

[55] VIMBELA G V, NGO S M, FRAZE C, YANG L, STOUT D A. Antibacterial properties and toxicity from metallic nanomaterials [J]. International Journal of Nanomedicine, 2017, 12: 3941−3965.

[56] RAD GOUDARZI M, BAGHERZADEH M, FAZILATI M, RIAHI F, SALAVATI H, SHAHROKH ESFAHANI S. Evaluation of antibacterial property of hydroxyapatite and zirconium oxide-modificated magnetic nanoparticles against *Staphylococcus aureus* and *Escherichia coli* [J]. IET Nanobiotechnol, 2019, 13: 449−455.

[57] MÉNDEZ-PFEIFFER P A, SOTO URZÚA L, SÁNCHEZ-MORA E, GONZÁLEZ A L, ROMO-HERRERA J M, GERVACIO ARCINIEGA J J, MARTINEZ MORALES L J. Damage on escherichia coli and staphylococcus aureus using white light photoactivation of Au and Ag nanoparticles [J]. Journal of Applied Physics, 2019, 125: 213102.

羟基磷灰石与氧化锆体积比对
钛基复合支架力学性能和腐蚀性能的影响

Mehmet TOPUZ[1], Burak DIKICI[2], Mehmet GAVGALI[3], Yasemin YILMAZER[4]

1. Department of Mechanical Engineering, Van Yüzüncü Yıl University, Van 65080, Turkey;
2. Department of Metallurgical and Materials Engineering, Atatürk University, Erzurum 25240, Turkey;
3. Department of Mechanical Engineering, Necmettin Erbakan University, Konya 42090, Turkey;
4. Department of Molecular Biology and Genetics, İstanbul Sabahattin Zaim University, İstanbul 34303, Turkey

摘　要：通过环保、低成本的混合法制备氧化锆(ZrO_2)和羟基磷灰石(HA)增强钛基支架材料，该材料具有较低的弹性模量(E)、足够的物理、电化学和生物学性能。研究羟基磷灰石和氧化锆体积分数的变化对支架力学性能、腐蚀性能和抗菌性能的影响。采用扫描电子显微镜结合电子色散光谱和 X 射线衍射对支架进行表征，通过压缩试验检测材料的力学性能及其详细的断裂机制，用电化学法测试样品在 37 ℃模拟体液中的体外腐蚀敏感性，通过比较大肠杆菌和金黄色葡萄球菌的抑菌面积进行抑菌试验。结果表明，随着 HA:ZrO_2 体积分数比例的增加，支架的力学强度降低，当其比例为 6:4 时，复合支架的 E 最低(6.61 GPa)。纯钛、HA:ZrO_2 体积分数比例为 3:2 和 6:4 的支架材料，其腐蚀电流密度(J_{corr})分别为 21、337 和 504 μA/cm^2。体积分数比例为 6:4 的支架对金黄色葡萄球菌的抑菌能力优于其他支架。

关键词：钛生物复合材料；羟基磷灰石；氧化锆；支架；力学性能；体外腐蚀

(Edited by Bing YANG)